INTERNATIONAL JOURNAL OF COMPUTER INTEGRATED MANUFACTURING
https://doi.org/10.1080/0951192X.2024.2314783

Taylor & Francis
Taylor & Francis Group



# The role of tool path on microstructure uniformity in large-format additive manufacturing: integrated thermo-metallurgical-mechanical approach

Jakub Mikula[a], Rajeev Ahluwalia[a], Athanasius Louis Commillus[a], Kai Ren[b,c], Youxiang Chew[b], Guglielmo Vastola[a] and Yong-Wei Zhang[a]

[a]Institute of High Performance Computing (IHPC), Agency for Science Technology and Research (A*STAR), Singapore, Republic of Singapore; [b]Singapore Institute of Manufacturing Technology (SIMTech), Agency for Science Technology and Research (A*STAR), Singapore, Republic of Singapore; [c]State Key Laboratory of Fluid Power and Mechatronic Systems, School of Mechanical Engineering, Zhejiang University, Hangzhou, Zhejiang, PR China

**ABSTRACT**

Directed energy deposition (DED) of large metal components has clear potential to revolutionise supply chains in several sectors, including marine & offshore and oil & gas. To insert this technology in production, ensuring part quality and consistency is of primary importance. However, such insertion is hindered by bottleneck issues arising from the manufacturing process, including part distortion and non-uniform mechanical properties. To address this important industrial need, an integrated thermo-metallurgical-mechanical numerical model capable of directly reading the robot tool-path (g-code) as well as the component shape, is here developed in-house and tailored to steel EH36, which is of particular relevance to the marine, offshore and oil & gas sectors. The model computes temperature at part scale, microstructure (phase fraction distribution) and residual stress and distortion, where each step of the chain is informed by the previous one. After demonstrating the framework on a single bead and thin wall geometries, the framework is applied to investigate the role of tool path in printing a more complex geometry. The presented framework allows to digitally correlate part design, process parameters, and tool path with microstructure distribution, residual stresses, and distortion, supporting digital process development in DED of large metal components.

**ARTICLE HISTORY**
Received 19 June 2023
Accepted 21 January 2024

**KEYWORDS**
Directed energy deposition; multi-physics modeling; thermo-metallurgical-mechanical analysis; design for additive manufacturing; EH36; finite element analysis

## 1. Introduction

Transition to decentralized manufacturing and agile supply chain is a recent global trend where manufacturing is closer to the point of use, encompassing all verticals of first-time manufacturing, re-manufacturing (Kaierle et al. 2017) and replacement of obsolete parts (Bonnín Roca et al. 2019). Due to its ability for customisation and modular deployment, additive manufacturing is the ideal process to enable such manufacturing paradigm shift (Dietrich, Kenworthy, and Cudney 2019).

A practical example of distributed manufacturing is in the shipbuilding sector. In this sector, additive manufacturing is being explored as the end-point for (re)manufacturing of large metal components (Strickland 2016) including propellers (Ya and Hamilton, 2018), because it has the potential to significantly reduce the procurement time for new parts, from months to weeks, therefore reducing the idle time of marine equipment. Due to the large size of such components, Directed Energy Deposition (DED) is emerging as an attractive advanced method to manufacture such parts. In this manufacturing process, an industrial robot mounts a material delivering system as its functional payload. In the delivery system, material is fed either in the form of wire or blown powder. Energy source for melting is typically provided by wire-arc electric discharge or by coaxial laser. The component is built by feeding the robot with a g-code containing the toolpath (sequence of robot moves) which specifies the process parameters, such as laser power and feed rate, at each time interval. A comprehensive review of the DED process, including its state of the art, has recently been published by Costello et al. (2023).

Large shipbuilding components are typically manufactured using steel of grade EH36. This alloy is a high-strength, austenitic steel with good corrosion resistance and weldability characteristics (Zou et al. 2018). At room temperature and for the case of forging, the

**CONTACT** Jakub Mikula mikulaj@ihpc.a-star.edu.sg; Guglielmo Vastola vastolag@ihpc.a-star.edu.sg
Supplemental data for this article can be accessed online at https://doi.org/10.1080/0951192X.2024.2314783.

microstructure is primarily composed of ferrite and bainite, together with a small fraction of martensite (Han et al. 2011). Because of its low carbon content, EH36 is also applicable to additive manufacturing, justifying the research into large-format DED as a viable decentralised manufacturing solution for the maritime and shipbuilding sector (Wang et al. 2021).

However, obtaining successful and repeatable additive manufacturing builds of large metal components is a grand challenge. In fact, the local cooling rates and thermal gradients affect the local microstructure, which in turn affects the local mechanical properties and ultimately local residual stresses and distortion (Zheng et al. 2019). If distortions become too large, they may affect part quality to the point of significant deviations from designed tolerances, or even lead to fracture. Such bottleneck issues are particularly acute when manufacturing large components, due to the significant waste of funds, equipment and material if a large part fails midway during the build. To address such challenge, modeling and simulation offer a cost-effective approach to assess part quality before actual printing through virtualisation of the DED process. For this reason, developing a simulation capability which addresses large-format additive manufacturing by revealing the coupled role of thermal history and microstructure in dictating the part's mechanical response to process is of paramount importance.

Early numerical work on modeling DED was reported by (Labudovic, Dongming, and Kovacevic 2003) in three dimensions, who studied the thermal response of the part during processing. Comparison with thermal analytical modelling was done by (Peyre et al. 2008), where results were compared with numerical modeling. A large body of work on thermo-mechanical modeling was done by (Gouge and Michaleris 2018), where a thermal solver was coupled to a mechanical solver, not informed by microstructure (Heigel, Michaleris, and Reutzel 2015). Such capability was also demonstrated by (Yang et al. 2016) as well as by (Stender et al. 2018) where quasi-static simulations were explored to reduce the computational cost. Further work was done by (Chiumenti et al. 2017) who performed sensitivity analysis which showed the quantitative role of each process parameter in determining the temperature field. Thermo-mechanical modelling with finite elements including the role of fluid flow was reported by Chew *et al*. for AISI 4340 steel (Chew et al. 2015) for single and multiple beads at the scale of the melt pool, while Ren *et al*. later used the same approach to study the role of toolpath on rectangular clad layers (Ren et al. 2019). Because of the need to describe the microstructure at the scale of the whole component, microstructure models typically emply analytical formulations whereby microstructural features (such as phase fractions) are scalars attached to each integration point of the mesh. Here, formulations include the Johnson-Mehl -Avrami-Kolmogorov (JMAK) Avrami (2004), Koistinen-Marburger (Koistinen and Marburger 1959) or Leblond (Leblond and Devaux 1984). In these models, variables are evolved at each time step where inputs are typically the local temperature, cooling rate, and microstructure. Because these models involve time integration of analytical expressions, they do not require significant computational cost and are thus particularly suited to be integrated with finite element calculations. Implementation of a thermo-metallurgical model, without implementation of a mechanics coupling, was demonstrated by (Weisz-Patrault 2020) for stainless steel 316 L, where the material model was formulated in terms of Johnson-Mehl-Avrami-Kolmogorov (JMAK) equations. This work combined a thermal solver with a metallurgical model to enable investigation of process-property correlations as earlier envisaged by (Costa et al. 2005). In a similar line of thought, (Lu et al. 2022) worked on Ti6Al4V alloy with an in-house thermo-mechanical framework and studied the role of baseplate as well as process parameters in the overall residual stress and microstructure uniformity, albeit without the explicit incorporation of a microstructure model. Conversely, Baykasoğlu *et al*. demonstrated a thermo-metallurgical model for Ti6Al4V, without a mechanical solver, based on the ABAQUS finite element framework (Baykaso˘glu et al. 2020). Recently, (Merve et al. 2023) presented a thermo-metallurgical-mechanical implementation for the Ti6Al4V material system, and applied it to components of simple rectangular shape. In terms of the steel material system, prior work was done by (Han et al. 2011) for the case of butt welding, whereby a metallurgical model accounted for the relevant phases and was validated with Continuous

Cooling Transformation (CCT) data, while no attempt was made to include it in a DED process modelling. Thermo-mechanical modelling, without a microstructure model, was also recently demonstrated by Ali *et al*. using the phase field method to model melting and solidification and implemented in the FEniCS framework (Ali, Heider, and Mark 2023). An early exploration of the role of tool path in influencing part distortion was reported by Lu *et al*. for Ti6Al4V, using a validated thermo-mechanical model in simple rectangular shapes (Lu et al. 2020). Overall, the prior body of work illustrates that, while some attempts have been made to integrate different modelling capabilities for DED process, none of them are capable of addressing the role of microstructure in dictating mechanical properties, residual stresses, and distortion in EH36 steel and for complex-shaped components, while being able to predict how the choice of tool path influences the final part's properties.

In this work, the formulation and numerical implementation of a sequentially coupled thermo-metallurgical-mechanical solver tailored to EH36 steel is reported, and implemented in a fully in-house software application. Thanks to such in-house development, the capability to read arbitrary g-code tool paths is included. As a result, using this framework, the exploration of the role of different tool paths in influencing the local part microstructure and, in turn, local mechanical properties and distortion is demonstrated. This framework provides a monolithic tool to develop process parameters, part design, or both, to improve microstructure uniformities and explore residual stress localisations. The paper is organised as follows. In Section 2, the mathematical description of the model and its components is laid down. In Section 3 the material properties used in the simulation are summarised. In Section 3 a series of simple illustrative simulation cases as a model verification exercise are presented. In Section 4 the printing process of a more complex geometry and the effect of the toolpath on its thermal, metallurgical, and mechanical response are shown. Finally, a summary and conclusions are reported in Section 5.

## 2. Model formulation and implementation

Illustration of the framework begins by laying down the pseudo-code of the sequential thermo-metallurgical-mechanical model, as shown in Alg. 2, followed by a detailed description of the individual solvers.

**Algorithm 1** Part-scale simulation platform workflow.

**while** unsatisfying result **do**
**Require**: STL file $\Omega_{STL}$ (component, baseplate)
**Require**: g-code file (SIEMENS Sinumerik format)
**Require**: material
**Require**: boundary conditions
  Domain voxelization: $\Omega \leftarrow$ STL file
  Block subdivision: $\Omega_b \in \Omega \leftarrow$ g-code file toolpath
  **for** $i < N_b$ **do**
  $\theta(\vec{x},t) \leftarrow q_s(\vec{x},t), \vec{x} \in \cup_{j\le i}\Omega_j$ ▷THERMAL SOLVER
  $\xi_i(\vec{x},t) \leftarrow \theta(\vec{x},t), \vec{x} \in \cup_{j\le i}\Omega_j$ ▷METALLURGICAL SOLVER
  $\boldsymbol{u}(\vec{x},t), \sigma(\vec{x}_i,t) \leftarrow \theta(\vec{x},t), \xi_i(\vec{x},t), \vec{x} \in \cup_{j\le i}\Omega_j$ ▷MECHANICAL SOLVER
  **end for**
**end while**

The implemented algorithm represents a sequential multi-scale approach to predicting the temperature field $\theta(\vec{x},t)$, volume fractions of individual phases $\xi_i(\vec{x},t)$ and the displacement field $\vec{u}(\vec{x},t)$ with the residual stresses $\sigma(\vec{x},t)$. The algorithm begins with loading the STL file, g-code file and material input file with the boundary conditions and solving the presented set of equations on the discretized domain of $\Omega_{STL}$ which is partitioned into blocks $\Omega_b$.

The set of process parameters is read from the g-code file as defined by the SIEMENS Sinumerik format (SIN 2018). Each line of the g-code is converted into tool-path coordinates $\vec{x}$, speed $\vec{v}$, and laser power $P$. Information such as axis transformation, repetitive cycle, positioning and others are also accounted for in order to capture the correct time intervals between the movements with the laser power 'on' and 'off'. This way, the complete printing strategy is loaded. The geometry is read from STL files for both the component and the baseplate. After having assigned material properties and boundary conditions, the domain is discretized, followed by spatio-temporal simulations of the printing process and the cool-down step after printing. In the next sections, each solver is discussed individually, followed by results and discussion of the integrated analysis.

### 2.1. Thermal solver

In order to evaluate the temperature field $\theta(\vec{x})$ and the thermal history $\theta(t)$ during the build, the following heat equation is solved:

$$\begin{aligned} \rho(\theta)c_p^*(\theta)\frac{\partial\theta(\vec{x},t)}{\partial t} &= \cdot[k(\theta)\ \theta(\vec{x},t)] + q_h(\vec{x}_\Gamma,\theta) + q_s(\vec{x},t) \\ q_h &= -\frac{hA_\Gamma}{V_\Omega}(\theta-\theta_\infty), \vec{x}\in\Gamma \\ q_s &= \begin{cases} \frac{\mathcal{A}P}{V_{\Omega_b}} & \text{if} \quad \vec{x}\in\Omega_b \\ 0 & \text{otherwise} \end{cases} \end{aligned}, \quad (1)$$

where $\rho$ is the material's density, $c_p^*$ is the apparent specific heat capacity, $k$ is the thermal conductivity and $q = q_h + q_s$ is the volumetric heat rate either due to the Newtonian convection from the surface ($q_h$) or due to the focused heat source (such as laser) ($q_s$). Additionally, $\theta_\infty$ is the ambient temperature, $\mathcal{A}$ is the absorptivity coefficient and $P$ is the laser power. Equation 1 is solved using the finite element method making it applicable to complex geometries that are often encountered in additive manufacturing.

The apparent specific heat is defined as:

$$c_p^*(\theta) = c_p(\theta) + L\frac{\partial f}{\partial\theta}, \quad (2)$$

with the volume fraction of liquid is approximated as

$$f = \begin{cases} 1 & \theta \geq \theta_L \quad \text{liquid} \\ \frac{\theta-\theta_S}{\theta_L-\theta_S} & \theta_S < \theta < \theta_L \quad \text{mushyzone} \\ 0 & \theta \leq \theta_S \quad \text{solid} \end{cases}. \quad (3)$$

Here, $\theta_L$ and $\theta_S$ are the liquidus and solidus temperatures, respectively, and $L$ is the latent heat of phase transformation.

The heat equation is solved in discrete time steps $\Delta t$, each with a different geometrical configuration approximating the continuous deposition of material. The spatial discretization is schematically illustrated in Figure 1.

Beginning with the domain of the STL file $\Omega_{STL}$ (one for the component and one for the baseplate) and the choice of the voxel size, the algorithm first performs a voxelization $\Omega_{STL} \rightarrow \Omega$. This functionality is performed by first generating a structured grid of the size of the domain outline and then removing the voxels outside of $\Omega_{STL}$ and renumbering the voxels that remain. This process generates the finite element mesh. Unlike the powder-bed fusion process where the material deposition can be simulated by activating layers of finite elements, here the process is more complex and the element activation sequence needs to follow the robot toolpath.

To model material deposition, the mesh is discretized into blocks of voxels ($\Omega_b(i)$, $i = 1, 2, \ldots, N$) which are activated in the sequence following the path given by the g-code. In this implementation, the shape of the block is generated by either a circle or an ellipse travelling and activating the voxels along the g-code path for a given time interval $\Delta t$ (see illustration in the upper right corner of Figure 1). The blocks may also overlap with each other since each voxel may be assigned to more than one $\Omega_b(i)$. The spherical or ellipsoidal representation of the deposited solid surface was chosen after observed shapes (Kaierle et al. 2017; Ren et al.) and should suffice the part-scale simulation level. In terms of the heat equation, an assumption is made that the heat source $q_s$ is distributed uniformly within each newly activated block. The total amount of energy that is applied to the system then remains the same irrespective of the number of blocks.

The shape of each voxel is approximated using bilinear shape functions that are used for the finite element analysis (Belytschko, Liu, and Moran 2000). The temperature field is approximated as $\theta(\vec{x},t) \approx \varphi_i(\vec{x})\theta_i(t)$, together with $\theta_\infty(\vec{x}) \approx \bar{\varphi}_i(\vec{x})\theta_{\infty_i}$ where $\varphi_i(\vec{x})$ and $\bar{\varphi}_i(\vec{x})$ are the three- and two-dimensional shape functions, respectively. The finite

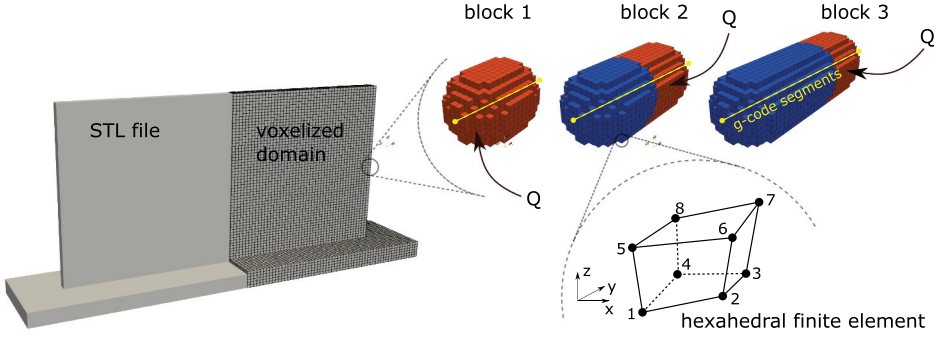


Figure 1. A schematic illustration of the 3-level discretization scheme of the domain of the STL file: (1) voxelization of the domain, (2) division of the voxelized domain into (possibly overlapping) blocks of finite elements, (3) hexahedral finite elements.

element discretization of Eq. 1 results in a system of linear differential equations that can be written in the following matrix format:

$$\boldsymbol{M}\dot{\theta} + \boldsymbol{K} = \boldsymbol{Q_s} - \boldsymbol{H}_\Gamma(\theta - \theta_\infty), \tag{4}$$

where $\boldsymbol{M}$ is the capacitance matrix, $\boldsymbol{K}$ is the conductance matrix, $\boldsymbol{Q}_s$ is the heat source vector and $\boldsymbol{H}_\Gamma$ is the convection matrix. Using the fully implicit Euler method, the solution for the temperature field $\theta^{t+\Delta t}$ can be found at each time step by solving the system of linear algebraic equations:

$$\begin{array}{lll} \mathcal{K}\theta^{t+\Delta t} & = \mathcal{F} & \\ \mathcal{K} & = M + \Delta t(K + H_\Gamma) & , \\ \mathcal{F} & = M\theta^t + \Delta t Q_s + \Delta t H_\Gamma \theta_\infty & \end{array} \tag{5}$$

where $\mathcal{K}$ denotes the global matrix and $\mathcal{F}$ the global vector.

### 2.2. Metallurgical solver

To account for modeling both the displacive and the diffusive phase transformations in steels such as EH36, a combination of the Koistinen-Marburger (Koistinen and Marburger 1959) and Leblond (Leblond and Devaux 1984) models is employed to simulate the microstructure evolution at part-scale. While earlier studies have focused mostly on simple continuous cooling simulations (Han et al. 2011; Kooiker, Perdahcıoğlu, and van den Boogaard 2020; Rong et al. 2018; Weisz-Patrault 2020), the objective of this work is to assess the suitability of such framework in simulating the process of directed energy deposition where the material point generally undergoes a large number of heating-cooling cycles.

The following form of the Koistinen-Marburger equation (Koistinen and Marburger 1959) is adopted:

$$\begin{array}{l} \xi_M^c = 1 - \exp(-\beta_M(M_s - \theta)) \\ \xi_i^h = 1 - \exp(-\alpha_i(A_f - \theta)) \end{array} , \tag{6}$$

where $\xi_M$ is the volume fraction of martensite and $M_s$, $A_f$ are the martensite start and austenite finish temperatures, respectively. The superscripts $c$ and $h$ indicate cooling and heating, respectively. The constants $\alpha$ and $\beta$ are material parameters which can be calibrated from the known martensite finish and austenite start temperatures (Han et al. 2011).

Additionally, it is assumed a critical cooling rate of martensite phase transformation, $\dot{\theta}_c^M$, above which the transformation is inhibited. To avoid sharp transitions in the phase volume fraction near the values of the critical cooling rate, the cooling portion of Eq. 6 is smoothed by assuming the following weight factor $w$:

$$\begin{array}{l} \xi_M^c = w[1 - \exp(-\beta(M_s - \theta))] \\ w = \frac{1}{2}\left(\tanh\left(\frac{|\dot{\theta}| - \dot{\theta}_{c_M}}{\delta_M} + 1\right)\right) \end{array} , \tag{7}$$

where $\delta$ is a parameter related to the uncertainty of the value of the critical cooling rate, while a sharp transition can be recovered for $\delta \to 0$. Given the diffusionless nature of the martensitic transformation, this model is athermal. In order to apply the model to an arbitrary heating-cooling thermal history, the model is implemented in rate (incremental) form during the cooling parts,

$$\Delta\xi_M = w[-\beta_M \exp(-\beta_M(M_s - \theta))]\Delta T, \tag{8}$$

and analogously during the heating parts of the thermal history.

On the other hand, regarding the diffusion-driven phase transformations, the following form of the Leblond's model is adopted (Leblond and Devaux 1984):

$$\dot{\xi}_i = w_i \left[\frac{\xi_i^{eq}(\theta, \dot{\theta}) - \xi_i}{\tau_i(\theta, \dot{\theta})}\right], \tag{9}$$

where $\xi^{eq}$ represents the equilibrium volume fraction (which may not necessarily be reached, but is tended to) and $\tau$ represents a time-scale parameter dictating the rate of the kinetics. These parameters are usually a function of both the temperature $\theta$ and the temperature gradient $\dot{\theta}$ (Leblond and Devaux 1984). In line with the previous equations, here, the weight is also introduced

$$w_i = \begin{cases} -\frac{1}{2}\left(\tanh\left(\frac{|\dot{\theta}| - \dot{\theta}_{c_i}}{\delta_i} + 1\right)\right) + 1 & \text{if} \quad \dot{\theta} < 0 \\ 1 & \text{if} \quad \dot{\theta} \geq 0 \end{cases}, \tag{10}$$

where the phase transformation takes place only above a certain critical cooling rate. The sharp (unphysical) transitions are recovered for $\delta \to 0$. A flow chart illustrating the implementation of algorithm is provided in A1.

It is now illustrated that a combination of the two models (Eq. 6 and Eq. 9) is capable of predicting a CCT (continuous-cooling-transformation) diagram depicting all four major phases of EH36 assumed in this work (austenite, martensite, ferrite and bainite).

Solutions for single-point continuous cooling conditions are presented in Figure 3(a). These predictions, albeit for simple cooling rate conditions, are in good agreement with literature (Han et al. 2011): At low cooling rates, ferrite becomes the dominant phase. A mixture of ferrite and bainite appears at higher cooling rates which is then substituted by martensite at the rates that favour displacive phase transformations.

Due to the difficulty of gathering experimental data for an arbitrary heating-cooling cycle, it is assumed that a material point obeys Eq. 6 for martensite and Eq. 9 for ferrite and bainite during the cooling step and Eq. 6 for all phases during the heating step. This is motivated by the fact that the average heating rates in additive manufacturing upon material melting are usually even faster than the subsequent cooling rates during material solidification, which may allow for diffusion-driven processes.

Based on this formulation, dilatometry curves are generated beginning with heating of the martensite followed by cooling with various cooling rates (presented in Figure 3b). The model parameters and transformation strains are estimated based on the literature of similar steels (Leblond and Devaux 1984; Lee, Lusk, and Lee 2007; Piekarska, Kubiak, and Zmindak 2017).

### 2.3. Mechanical solver

The objective of the mechanical solver is to predict the distortion and residual stresses given the thermal history as well as phase volume fraction evolution. The solver is established based on the same three-level discretization scheme as introduced in Figure 1.

Assuming small grain size with random texture, an isotropic constitutive model is implemented with phase- and temperature-dependent Young's modulus and Poisson's ratio:

$$\dot{\sigma} = \mathbb{C}(\xi_i, \theta) : \dot{\varepsilon}^{el}, \tag{11}$$

$$\mathbb{C} = \frac{E(\theta)}{1+\nu(\theta)}\boldsymbol{I} + \frac{E(\theta)\nu(\theta)}{(1+\nu(\theta))(1-2\nu(\theta))}(\mathbf{1}\otimes\mathbf{1}). \tag{12}$$

The total strain rate is additively decomposed into:

$$\dot{\varepsilon} = \dot{\varepsilon}^{el} + \dot{\varepsilon}^{thm} + \dot{\varepsilon}^{p}, \tag{13}$$

where the total strain $\varepsilon_{ij} = \frac{1}{2}\left(\partial u_i/\partial x_j + \partial u_j/\partial x_i\right)$ is calculated from the displacement field $\vec{u}$. Individual components of the displacement field are denoted by $\vec{u} = (u, v, w)$. The thermo-metallurgical strain is given as $\varepsilon_{ij}^{thm} = \delta_{ij}(\theta - \theta_0)\sum_k \xi_k \alpha_k + \sum_k \xi_k \varepsilon_{ij}^0(k)$, and the plastic strain rate $\dot{\varepsilon}_{ij}^{p} = \dot{\lambda}\frac{\partial f(\xi_i,\theta)}{\partial \sigma_{ij}}$. The symbol $\delta_{ij}$ is used to denote the Kronecker's delta, $\alpha$ is the thermal expansion coefficient, and $\varepsilon_{ij}^0(k)$ is the phase transformation strain of k-th phase.

Furthermore, $\lambda$ is the scalar plastic multiplier and $f(\theta)$ represents the temperature dependent-yield surface. The von-Mises isotropic plasticity is employed:

$$f(\theta) = \sqrt{\sigma^{dev} : \sigma^{dev}} - \sqrt{\frac{2}{3}}\left[\sigma_y(\xi_i, \theta) + H(\xi_i, \theta)\bar{\varepsilon}^{p}\right], \tag{14}$$

where $\sigma^{dev}$ is the deviatoric part of the stress tensor, $\sigma_y$ is the yield stress, $H$ is the hardening coefficient and $\bar{\varepsilon}^{p}$ is the scalar equivalent plastic strain $\bar{\varepsilon}^{p} = \int_0^t \sqrt{\frac{2}{3}} \parallel \dot{\varepsilon}^{p} \parallel d\tau$.

The material model is solved using the standard predictor-corrector approach (Simo and Taylor 1985). The stress at the end of the increment is updated as $\sigma_{i+1} = \sigma_{i+1}^{tr} - \mathbb{C} : \Delta\lambda \frac{\partial f(\theta)}{\partial \sigma}|_{i+1}$ which, for an isotropic material, can also be expressed in its deviatoric form $\sigma_{i+1}^{dev} = \sigma_{i+1}^{dev^{tr}} - 2\nu(\theta)\Delta\lambda \frac{\partial f(\theta)}{\partial \sigma^{dev}}|_{i+1}$. Given the von-Mises yield surface, the standard radial-return method is recovered from which the scalar plastic multiplier increment can be derived:

$$\Delta\lambda = \frac{\sqrt{\sigma_{i+1}^{dev^{tr}} : \sigma_{i+1}^{dev^{tr}}} - \sqrt{\frac{2}{3}}(\sigma_y(\theta) + H(\theta)\bar{\varepsilon}_i^{p})}{2\nu(\theta) + \frac{2}{3}H(\theta)}. \tag{15}$$

The material non-linearity at the finite element scale is solved using the Newton–Raphson method that arrives at mechanical equilibrium $\nabla \cdot \sigma = 0$.

The temperature-dependent material properties (specifically, Young's modulus, Poisson's ratio, yield stress, and hardening coefficient) used in this work were implemented from literature (Han et al. 2011; Rong et al. 2018). To account for experimental uncertainty in the measurements, the values used in the simulations were taken as the average between these two sources (see the following section).

## 3. Summary of material properties

In this section, a concise summary of the material properties employed in the simulations is provided. The sources from which the data is derived are

**Table 1.** Constant thermal properties.

| Name | Variable | Value | Unit | Source |
|---|---|---|---|---|
| Solidus | $\theta_S$ | 1465.1 | °C | (M. H. Ali and Sung Han 2021) |
| Liquidus | $\theta_L$ | 1522.5 | °C | (M. H. Ali and Sung Han 2021) |
| Latent heat | $L$ | 251400.0 | J/kg | |

acknowledged, when available in existing literature. In cases where specific data is not readily obtainable, estimation of the material parameters was done by drawing upon the author's experience with the model to ensure that the simulated behavior closely matches that of comparable low-carbon steels.

Table 1 contains the solidus, liquidus and latent heat properties used in the thermal simulations. All temperature dependent properties in the thermal simulations, such as density, conductivity, and specific heat, are presented in Figure 2. Table 2 provides the Koistinen-Marburger coefficients, transformation strains and thermal expansion coefficients for the study phases – austenite, martensite, ferrite and bainite. These coefficients were deduced from calibrating the phase fraction model in predicting the dilatometry curves as presented in Figure 3(b). Table 3 lists the Leblond-Devaux model coefficients for different cooling rates used for prediction of the CCT diagram presented in Figure 3(a). Finally, the temperature dependent mechanical properties used in the mechanical simulations are presented in Figure 4.

## 4. Model verification by simulation of simple geometries

In-house C + + code was developed to efficiently implement and solve the governing equations that were outlined in the preceding sections. The following third-party libraries were used: Trilinos (Trilinos Project Team 2020) (12.12.1) for solving the system of linear equations, Eigen (Guennebaud et al. 2010) (3.3.7) for matrix and vector operations, and The Visualization Toolkit (VTK)

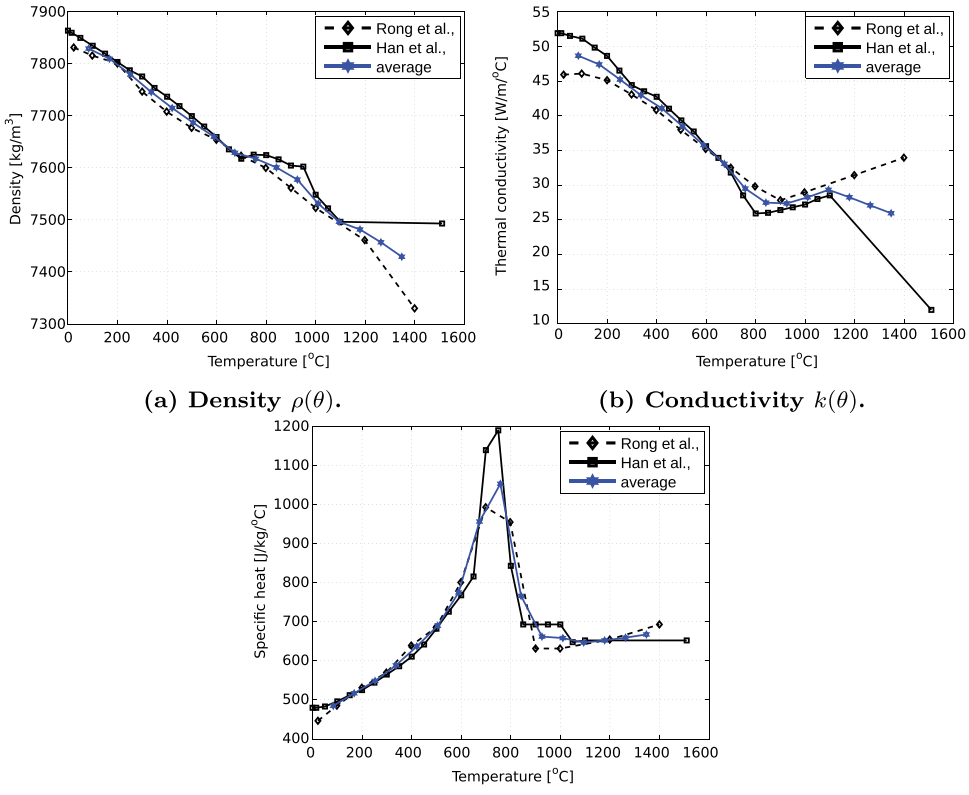


(a) Density $\rho(\theta)$. (b) Conductivity $k(\theta)$.

(c) Specific heat $c_p(\theta)$.

**Figure 2.** Temperature-dependent material properties of EH36 found in the literature, from (Han et al. 2011; Rong et al. 2018), together with their average (blue curves).

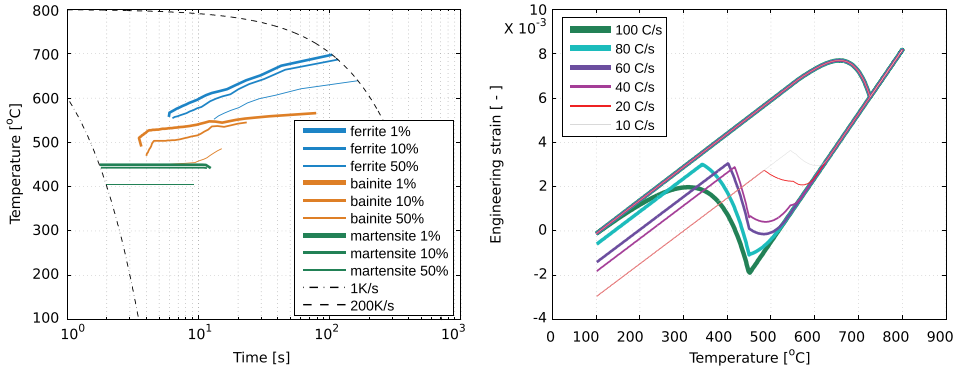


(a) Predicted CCT diagram with three product phases: ferrite, bainite, and martensite, showing the volume fraction at 1%, 10% and 50%.

(b) Predicted dilatometry curves (beginning with the martensite). Motivated by (Piekarska, Kubiak, and Żmindak 2017) (Lee, Lusk, and Lee 2007) (Leblond and Devaux 1984).

Figure 3. Predicted CCT and dilatometry curves.

Table 2. Koistinen-Marburger coefficients, transformation strains and thermal expansion coefficients (see Figure 3(b)).

| Koistinen-Marburger coefficients | | | | Transformation strains | | | Thermal expansion coefficients | | | |
|---|---|---|---|---|---|---|---|---|---|---|
| $\beta_M$ | $\alpha_M$ | $\alpha_F$ | $\alpha_B$ | $\Delta\varepsilon_M$ | $\Delta\varepsilon_F$ | $\Delta\varepsilon_B$ | $\eta_M$ | $\eta_F$ | $\eta_B$ | $\eta_A$ |
| 0.015 | 0.028 | 0.028 | 0.028 | 0.012 | 0.009 | 0.009 | 28.8e-6 | 14.9e-6 | 14.9e-6 | 14.9e-6 |

Table 3. Leblond-Devaux model parameters (Han et al. 2011). The values above and below critical cooling rates are denoted by '-'.

| $\partial\theta/\partial t$ | -0.98 | -1.74 | -2.58 | -5.08 | -10.71 | -16.72 | -20.46 | -29.35 | -41.67 | -65.29 | -84.3 | -100 |
|---|---|---|---|---|---|---|---|---|---|---|---|---|
| $\tau^F$ | 0.95 | 0.001 | 0.01 | 0.007 | 0.9775 | 1.2 | 1.95 | 1.8 | 1.055 | - | - | - |
| $\theta_s^F$ (°C) | 699.8 | 689 | 678.9 | 651.2 | 624.1 | 612.7 | 603.3 | 587.8 | 567.9 | - | - | - |
| $\theta_f^F$ (°C) | 581.2 | 570.4 | 567.8 | 562.2 | 555.5 | 545.8 | 550.1 | 546.7 | 543.7 | - | - | - |
| $\theta_s^B$ (°C) | 1.00E−04 | 1.00E−04 | 1.00E−04 | 1.00E−04 | 0.005 | 0.01 | 1.00E−04 | 1.44 | 1.51 | 0.787 | 2.42 | - |
| $\theta_f^B$ (°C) | 581.2 | 570.4 | 567.8 | 562.2 | 555.2 | 545.8 | 550.1 | 546.7 | 543.7 | 537 | 526.4 | - |
| $\theta_s^M$ (°C) | - | - | - | - | - | - | - | - | 450 | 450 | 450 | 450 |
| $\theta_f^A$ (°C) | 726.85 | 726.85 | 726.85 | 726.85 | 726.85 | 726.85 | 726.85 | 726.85 | 726.85 | 726.85 | 726.85 | 726.85 |

(Schroeder, Martin, and Lorensen 2006) (8.2) for unstructured grid representation, postprocessing, and rendering. The code was parallelized using OpenMPI (Gabriel et al. 2004) (4.0.5). The compiler was GNU `gcc` 9.4.0. All simulations were performed on a workstation with Intel® Xeon® CPU E5–2699 v4 @ 2.20 GHz processors. While the simulation time varies depending on the level of discretization, tool-path and geometry, the average computational time when running the simulations on 44 processors is of the order of 24 h for the thermal solver, 1 min for the metallurgical solver and 3 days for the mechanical solver.

### 4.1. Single bead

As a first case, cladding a single bead of EH36 on top of a baseplate that is of the same material is studied, with the intent to illustrate the maximum degree of resolution of the part-scale thermal solver that can be achieved using the presented framework. A single bead simulation is also useful as a fast exercise for calibrating the model that can later be applied to more complex geometries with reduced block size resolution (illustrated later in Sec. 4.2). The simulation setup consists of two STL files (baseplate and component) and a single line g-code segment. The deposition bead is of a radius of $r = 1.5$mm (and a layer height $h = r$). The baseplate dimensions are $120 \times 20 \times 4\text{mm}^3$. The effective laser power (with a constant absorptivity coefficient) $P^{eff} = 840$W is assumed, and the ambient temperature is fixed at $\theta_\infty = 300$K. The initial baseplate temperature is $\theta_\infty$. The convection coefficient is set to $h = 250\text{W/m}^2\text{K}$ on all surfaces. The speed of the printing head is

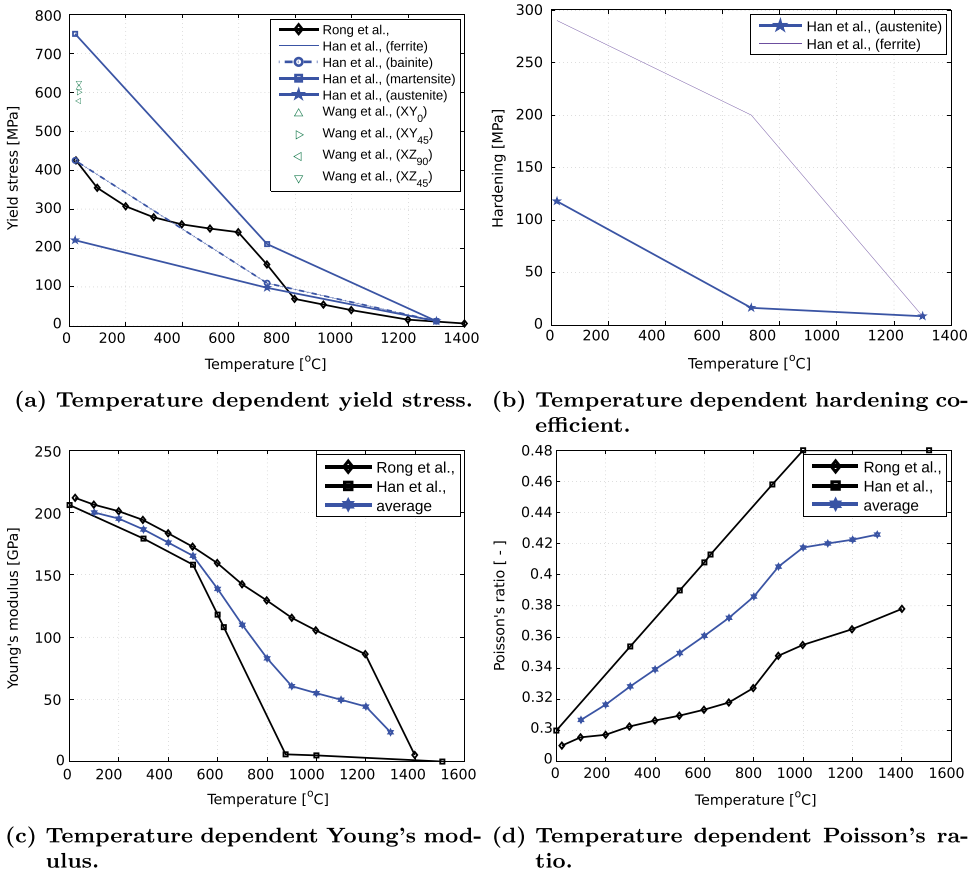


(a) Temperature dependent yield stress.

(b) Temperature dependent hardening coefficient.

(c) Temperature dependent Young's modulus.

(d) Temperature dependent Poisson's ratio.

**Figure 4.** Temperature dependent mechanical properties for EH36 obtained from refs (Han et al. 2011; Rong et al. 2018). The values used in the simulations were taken as an average between the two sources (blue curves).

1000mm/min, and the total printing time is 6 s. This is followed by a cool-down step simulated for 24 s. The simulation is performed with the voxel size of $0.25 \times 0.25 \times 0.25\text{mm}^3$ while the continuous deposition of material is discretized into 100 blocks. The small voxel size has been chosen to obtain a high resolution result of the temperature field. The block size sensitivity analysis will be presented later.

#### 4.1.1. Temperature field

The results of the temperature field evolution are presented in Figure 5. It is observed that during the course of simulation, a significant fraction of the total heat removal is due to the conduction through the baseplate (Figure 5(a)). After a short while, steady-state conditions are reached, and the region with the temperature of solidus attains a constant size and shape (Figure 5(b-c)). When the power is turned off, the temperature equilibrates with the ambient temperature (Figure 5(d)).

The complete thermal history was recorded at each node of the finite element mesh, saved to file in binary form, and passed to the metallurgical solver for the prediction of the phase fractions of austenite, ferrite, bainite, and martensite.

#### 4.1.2. Phase fractions

In the metallurgical solver, both the component and the baseplate may undergo phase transformation. For simplicity, the initial phase distribution within the baseplate is of equivalent fractions of ferrite, bainite, and martensite (each $^1/_3$ at every node). The results of the phase volume fraction at the end of the bead deposition (at $t = 6$s) are visualized in Figure 6. For a better visualization of the transformation within the baseplate, the samples are cut through the center with one half shifted upwards.

A careful inspection of Figure 6 reveals that the dominant phase transformation is from austenite into martensite. Interestingly, the solid-state phase

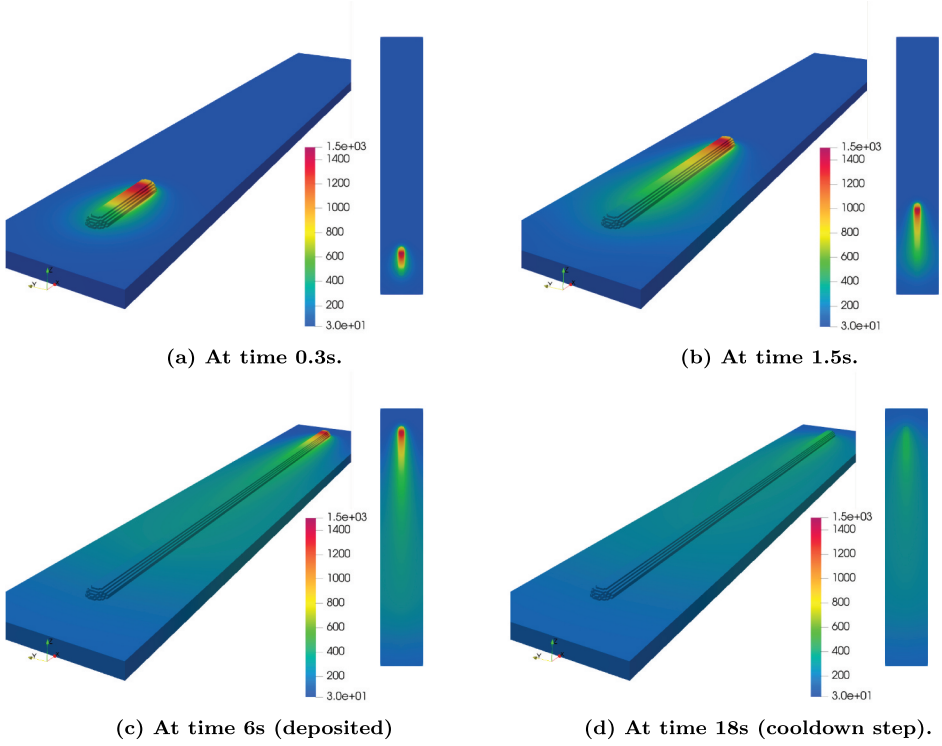


(a) At time 0.3s. (b) At time 1.5s.

(c) At time 6s (deposited) (d) At time 18s (cooldown step).

Figure 5. Single bead simulation depositing EH36 on top of the baseplate of the same material showing the evolution of the temperature field during the printing (a), (b), (c), and during the cool-down step (d). Units are in °C.

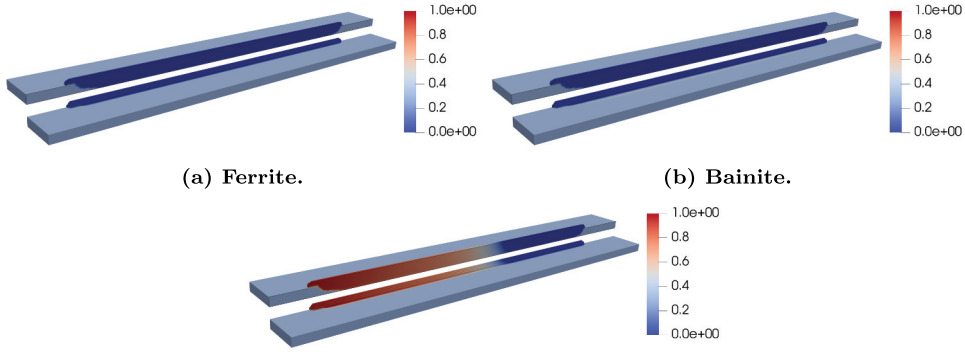


(a) Ferrite. (b) Bainite.

(c) Martensite.

Figure 6. Volume fraction of ferrite, bainite and martensite at the end of the bead deposition. For visualization purpose, the domain is cut through the centre with one half is shifted upwards.

transformation is also observed to take place within the baseplate (just below the deposited bead) where the temperatures rose above the $A_s$ leading to austenitization (front of Figure 6(c), followed by fast cooling and formation of martensite (left part of Figure 6(c)). The presence of large volume fraction of martensite can be explained by the high cooling rates when the hot material is first deposited onto the 'cold' baseplate. In this case, in fact, most of the heat is quickly conducted away through the baseplate, creating suitable conditions for the formation of martensite while leaving little time for the formation of other diffusion-driven phases.

#### 4.1.3. Distortion and residual stresses

Thermal and metallurgical information is passed to the mechanical solver for the prediction of distortion and residual stresses. Results of the mechanical solver in the mid-way of printing are presented in Figure 7. The mechanical solver is set up such that all the displacement degrees of freedom on the bottom plane of the baseplate are set to zero. The

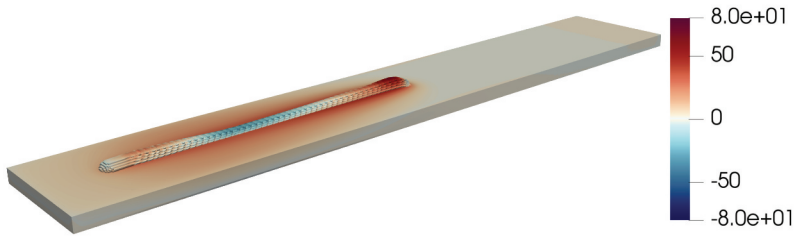


(a) Displacement field $w$ [$\mu$m].

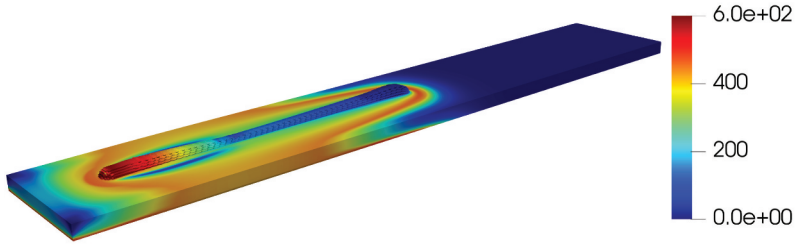


(b) Von-Mises stress [MPa].

Figure 7. Results of the mechanical analysis in the mid-way of printing. Deformation is 10× magnified.

remaining surface is assigned the natural traction-free boundary condition.

The deformation in Figure 7 is 10× magnified. The displacement field result in Figure 7(a) clearly indicates that the deposition of hot material on top of the cold baseplate initially causes expansion of the baseplate giving rise to the positive displacement component $w$ (front of the bead in Figure 7(a). As the material cools down, the bead starts to shrink as indicated by the negative displacement component $w$ in the central part of the bead. Eventually, the positive volume change due to martensitic transformation counteracts the shrinking strain (left part of Figure 7(a)). In complex geometries, such conditions may lead to interesting history of residual stresses or failure of the component.

As for the residual stresses in Figure 7(b), it is visible that the stress-bearing capacity of the hot material is close to zero. Eventually, as the material cools down, the residual stresses remain concentrated near the interface between the bead and the baseplate. This configuration creates tensile stresses along the length of the bead that would eventually lead to positive curvature of the system if the boundary displacement constrained is removed (illustrated in Fig. B1 in appendix).

## 4.2. Thin wall

Thin-wall experiments are relatively abundant in research of additive manufacturing, providing simple and fast source of reliable thermal and mechanical data that can be easily used for calibration of computational models (Bennett et al. 2018; Labudovic, Dongming, and Kovacevic 2003; Peyre et al. 2008). In this section, a thin wall is printed in line with the experiment presented by Bennett *et al.* (Bennett et al. 2018), albeit in the present case for EH36 instead of Inconel. An STL file of the thin wall was generated according to the experimental specifications stated in the paper.

The simulation set-up is schematically illustrated in Figure 8.

The domain in Figure 8 is discretized into voxels, each of the size of 0.5mm (see Figure 1) and subdivided into 1000 blocks following the g-code toolpath. A spherical representation of the block with radius $r = 1.5$mm is chosen and the height between the layers $h = 0.5$mm. The laser speed is set to $v = 1000$mm/min with the total printing time of $t = 16.5$min. The effective laser power is 900W.

### 4.2.1. Temperature field

The temperature field evolution during the printing is shown in Figure 9.

This simulation is an extension of the single bead simulation from the previous section. It is observed that, initially, a large portion of the heat is conducted through the baseplate, while in the later stage, with the increasing surface-to-volume ratio, through

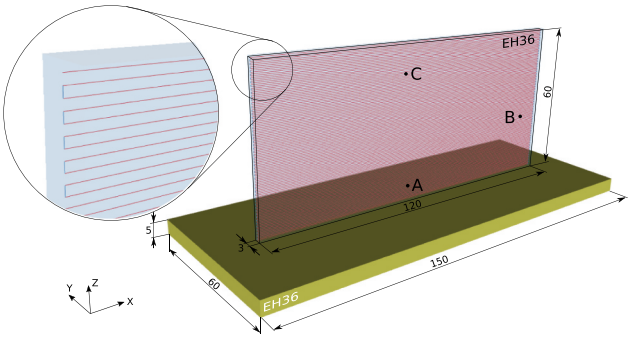


**Figure 8.** Simulation setup of the thin wall showing the 3D STL file of the component and based plate, and the g-code toolpath motivated by the experimental study (Bennett et al. 2018). All dimensions are presented in the units of mm.

convection from the surfaces. The temperature map profile in Figure 9 closely resembles the experimental data (Bennett et al. 2018) of a similar study.

A closer analysis of the complete thermal histories was performed for three points (A, B, and C) illustrated in Figure 8. The results are collated in Figure 10 (black curves labeled by '1000 blocks').

Our simulations are able to resolve every peak in line with the experimental results (Bennett et al. 2018). Each point is initially subjected to several heating-cooling cycles (with fast heating and cooling rates), the amplitude of which eventually attenuates subjecting each point to slow continuum cooling.

The advantage of the presented model lies in the flexibility of making the block size a user's choice. Because it is ensured that the total amount of energy entering the system is the same irrespective of the block size, one may choose a smaller block size to resolve the temperature details up to the melt pool boundary (see Figure 5) or a larger block size in order to reduce the computational cost. To elucidate this possibility, a sensitivity analysis of the block size for the wall printed with blocks {1000, 500, 100} was performed and illustrated in Figure 10.

The sensitivity analysis illustrates that high accuracy of the temperature field near the melt pool (first peaks of the thermal history) can only be achieved with a small block size ($\sim$ size of the melt pool). Nevertheless, while the prediction of the peak temperatures with the larger block size looses accuracy, it is still captured in an average sense. Importantly, the temperature profiles further away from the melt pool are not affected by the size of the block as seen in the later stage of the thermal history by the overlapping curves in Figure 10. Therefore, one can choose to compromise the accuracy for the computational time (which is proportional to the number of blocks, *i.e.*, to the number of iterations), depending on the purpose of the analysis. It should be noted that the block size sensitivity analysis presented in Figure 10 is

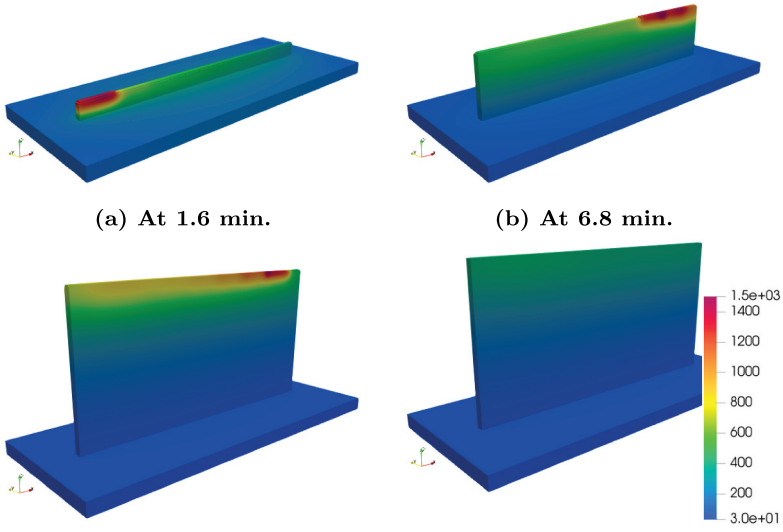


(a) At 1.6 min. (b) At 6.8 min.

(c) At 16.3 min. (d) At 16.8 min (beginning of cool-down step).

**Figure 9.** Temperature field evolution in the thin wall during printing and during the cool-down step. Total travelled distance is 14.5 m and total printing time is 16.5 min. Units are in Celsius degrees (°C).

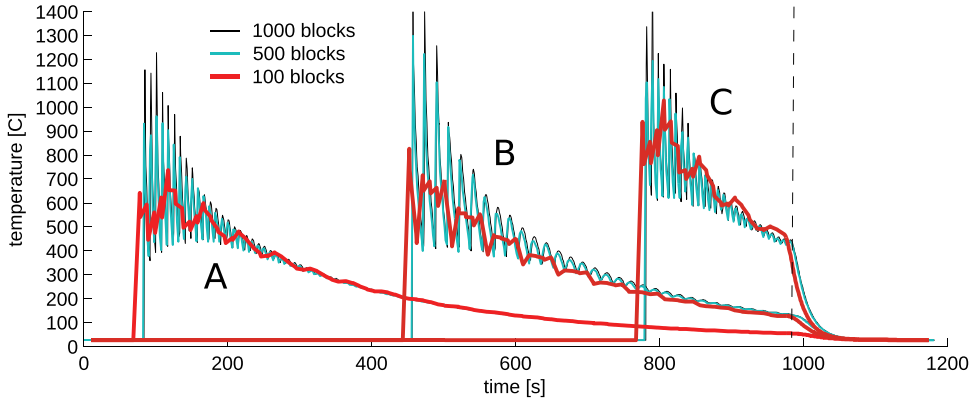


**Figure 10.** Thermal histories at points A, B, and C depicted in Figure 8 for the simulations of 1000 blocks (black), 500 blocks (green) and 100 blocks (red).

computed only for the thin wall geometry. It can be assumed that that choice of the optimal block size would depend on the complexity of the geometry and tool-path and would need to be investigated through such sensitivity analysis for each case.

### 4.2.2. *Phase fractions*

Following the thermal analysis, the results of the metallurgical solver are presented in Figure 11 depicting the phase fraction of ferrite (a), bainite (b) and martensite (c) in the as-built component (after the cooldown-step). A block size sensitivity analysis is included in C.

Initially, the phase transformation is dominated by the austenite → martensite transition where the cooling rates are relatively high due to the deposition of hot material on top of a cold baseplate. This was already illustrated in the single bead case in Sec. 4.1. Eventually, as the new material is deposited on top of the previously deposited thin wall, the temperatures remain relatively high and the cooling rates decrease. This allows sufficient time for the diffusive transformations (austenite → ferrite, and austenite → bainite) to take place. A fine mixture of ferrite and bainite dominates the central part of the thin wall. Finally, when the heat source is turned off, a small volume fraction

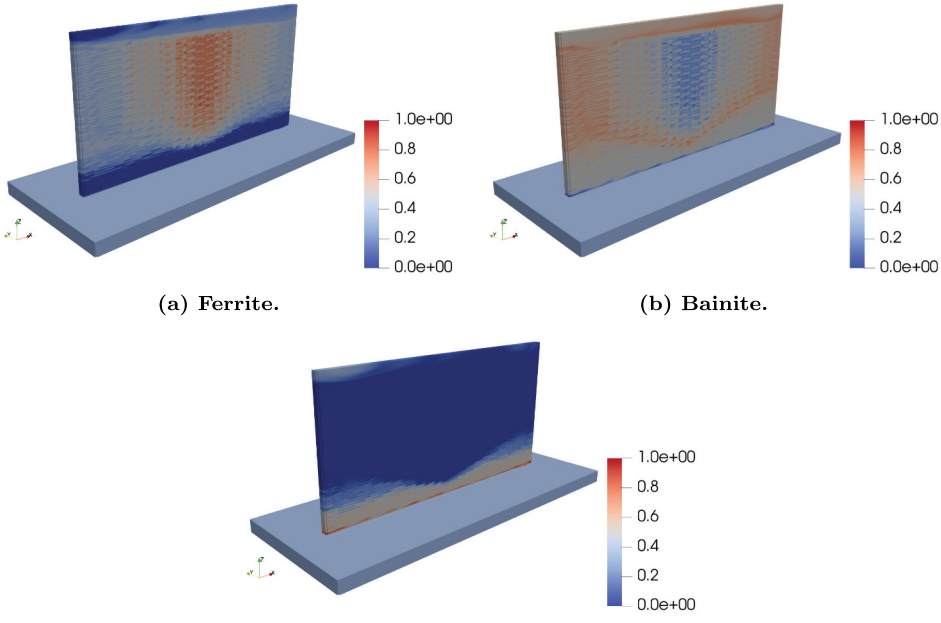


(a) Ferrite.

(b) Bainite.

(c) Martensite.

**Figure 11.** Volume fraction of ferrite, bainite and martensite in the as-built component.

of martensite appears near the top surface of the wall. A more detailed analysis of the temporal phase fraction evolution is presented for the A, B, and C points in Figure 12.

Point A in Figure 12(a) is situated near the interface between the martensite dominated region and the ferrite+bainite dominated region. As the printing progresses, the initially high cooling rates attenuate and the martensite ↔ austenite phase transformation is substituted by bainite and ferrite. The transformation stops once the critical cooling rates are reached (see CCT in Figure 3(a)) and when all austenite has fully transformed. Point A eventually consists of a mixture of ferrite, bainite and martensite.

The average cooling rates at point B in Figure 12(b) are relatively slower, and while small volume fraction of martensite is formed at the beginning, it is soon replaced by ferrite and bainite.

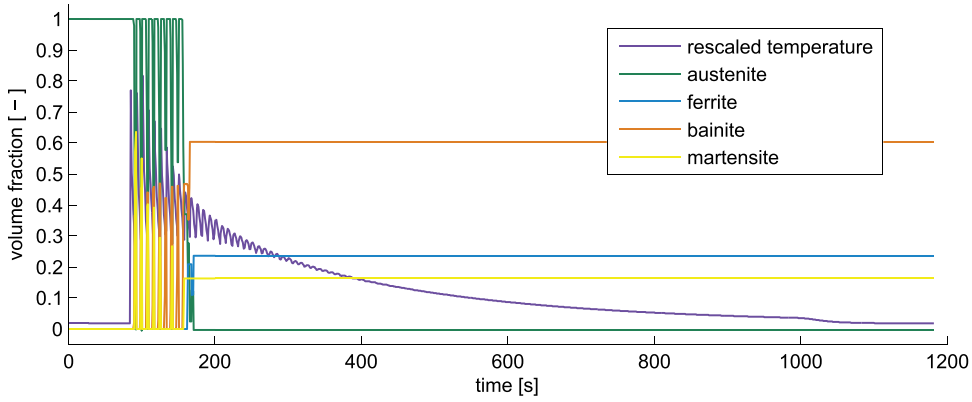


(a) Point A in Fig.8.

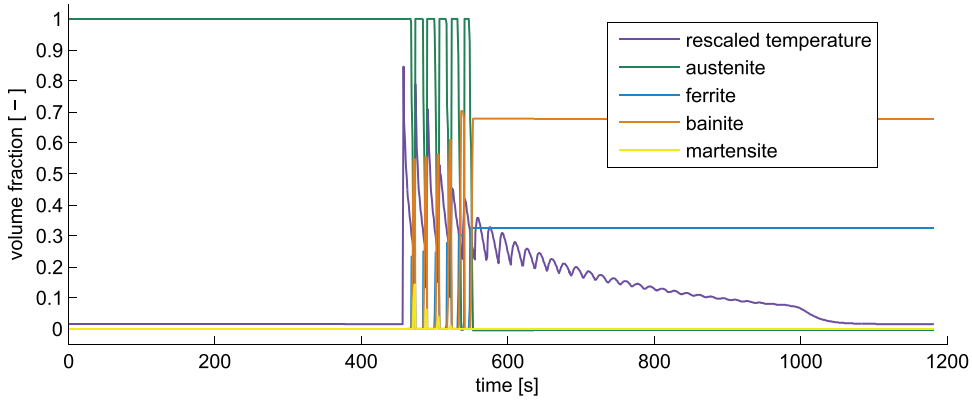


(b) Point B in Fig.8.

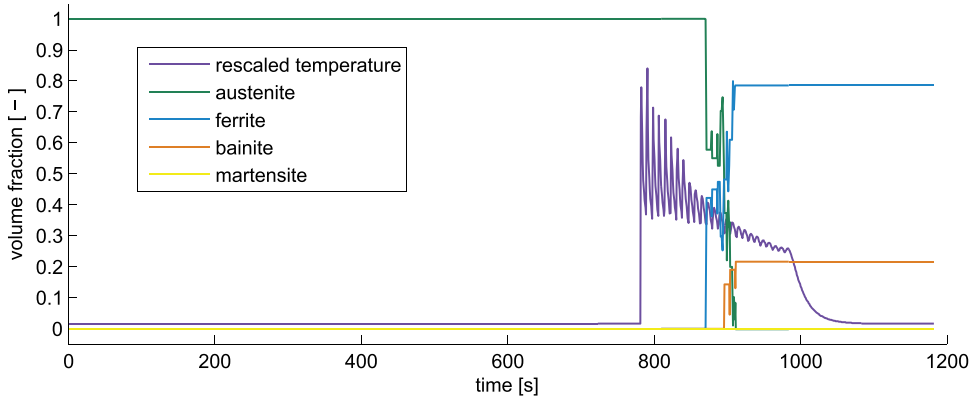


(c) Point C in Fig.8.

Figure 12. Phase volume fraction evolution of austenite, bainite, ferrite and martensite in the thin wall geometry at three distinct points. The re-scaled thermal history from Figure 10 is also included.

At point C in Figure 12(c), the average time between two subsequent passes is 12 of that at point B. Therefore, higher temperatures build up and slower cooling rates are expected. Such conditions are the most favourable for the formation of ferrite clearly visible also in Figure 11.

#### 4.2.3. Distortion and residual stresses

The collected thermal and metallurgical data are used to predict the distortion and residual stresses during printing. The stress components $\sigma_{xx}$, $\sigma_{yy}$, $\sigma_{zz}$ are presented in Figure 13, together with the deformed shape being 10× magnified.

The distortion and residual stress arise from the intricate history of phase transformation volume change and thermal shrinkage during the cooling. This is especially visible in the lower part of the thin wall that experiences the largest volume fraction of martensite. While the material initially shrinks due to the thermal strain it also expands during cooling by the means of austenite → martensite phase transformation creating the S-shape surface along the edge of the wall. The wavy surface pattern arises from the discrete phase fraction profiles (Figure 11) as well as from the numerical discretization and the spherical assumption of the deposited bead (as illustrated in Figure 1). The largest stresses appear near the baseplate.

## 5. Influence of toolpath

### 5.1. Thermal and metallurgical solver

In this section, the framework is applied to a more complex component having the shape of a 'windmill' to demonstrate the capability of the framework to reveal the role of the tool path in dictating the part's microstructure, distortion, and residual stresses. To this goal, two different g-codes were generated to build the component with a different sequence of robot moves. The tool paths are presented in Figure 14, where the first tool path builds the component in a uniform manner ('uniform' or 'reference' toolpath), while the second tool path localizes the robot movements within the domain of the STL file, (here denoted as 'optimized' tool path) with the aim of reducing the total printing time. The yellow lines in the figure indicate the segments with power 'on' and the red lines the segments with power 'off'. Clearly, as shown in Figure 14(b), the amount of robot movements that do not print is reduced significantly (total printing time reduction from 1.7h to 1h).

The toolpaths were generated using an automatic segmentation method by applying the following steps:

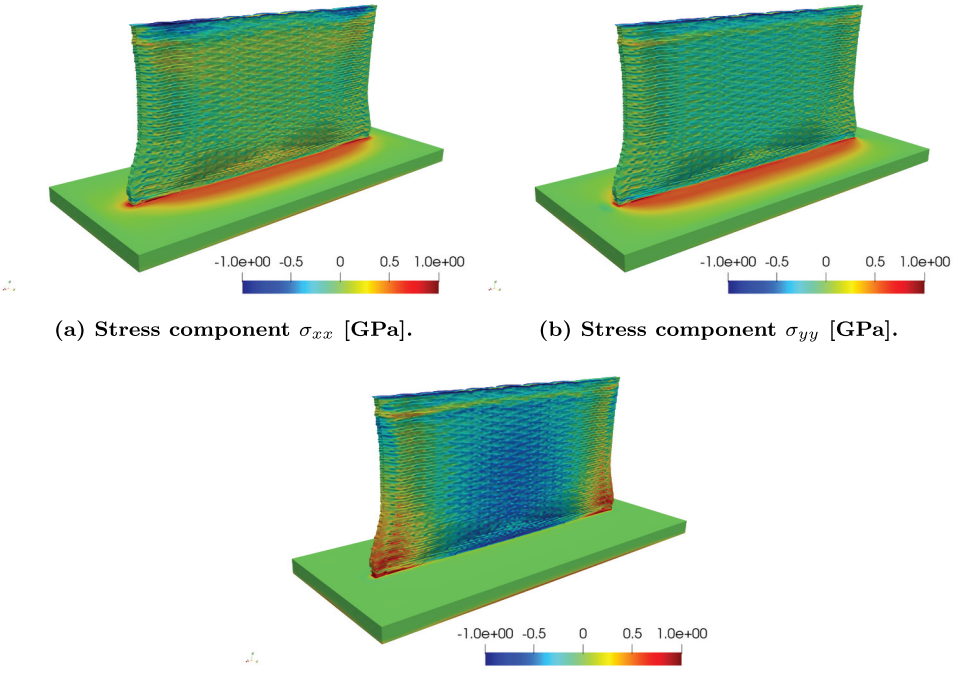


(a) Stress component $\sigma_{xx}$ [GPa]. (b) Stress component $\sigma_{yy}$ [GPa].

(c) Stress component $\sigma_{zz}$ [GPa].

Figure 13. Residual stress tensor components in the as-printed wall. Deformation is 10× magnified.

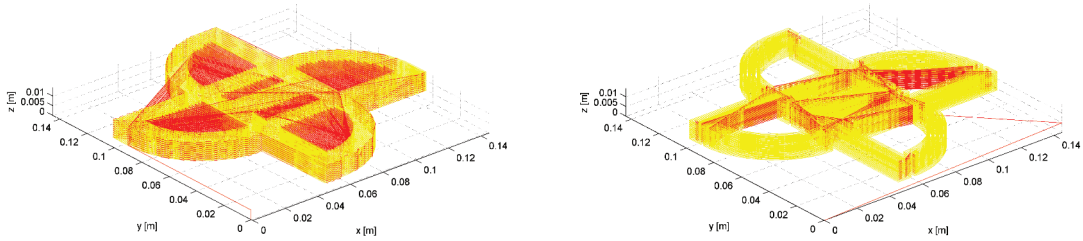


(a) Uniform toolpath pattern. Total traveled distance 93 m, total printing time 1.7 h.

(b) Optimized toolpath pattern. Total traveled distance 80 m, total printing time 1 h.

**Figure 14.** Windmill and cross geometry with two toolpath patterns. The yellow line segments illustrate the motion of the printing head when the power is on, and the red line segments illustrate the motion when the power is off.

(1) Generate the individual 2D layer from the original CAD model.
(2) Decompose the sliced 2D layer into a set of fundamental elements via extending line segments in the closed loop.
(3) Merge the remaining basic elements to generate the largest quasi-quadrilateral.
(4) Update the remaining basic elements set by deleting the elements in the quasi-quadrilateral generated in step 2.
(5) Repeat step 2–3 until no basic element remains.

The aforementioned method was designed by integrating empirical experience collected from the experiment to avoid short individual tool paths and turnings, improving the geometrical accuracy and mechanical properties of the deposited component. More information about the method can be found in (Liu et al. 2021).

In all simulated cases, the following configuration was chosen: average speed of the printing head $v = 1200\text{mm}/\text{min}$, effective laser power $P^{eff} = 1600\text{W}$, and the convection coefficient from the surface $h = 250\text{W}/\text{m}^2\text{K}$. The size of the deposited bead is set to $r = 1.5\text{mm}$. Additionally, the component is placed on top of a based plate (200mm × 200mm × 5mm) of the same material. These process parameters and sample positioning were typical for DED builds of EH36 (Wang et al. 2021). The simulation domain is discretized with the voxel size of 0.5mm and 1000 blocks. The time evolution of the temperature field is presented in Figure 15 for the uniform case and in Figure 16 for the optimized case.

In both cases, it can be observed that, initially, the applied heat is conducted through the baseplate, while in the later stage most of the heat is convected through the surface of the component. Note that the average temperatures are, on average, lower than the solidus temperature due to the block size that is larger than the expected melt pool size (see the sensitivity analysis in Figure 10).

Comparisons between Figures 15 and 16 also reveal the critical role of tool path in eliminating localized overheating of the component during the build. In the case of the uniform tool path, the component is generally given more time to convey the heat away during the time when the printing head moves across the empty space; however, strong heat localization is observed near the left and right edges of the windmill (see Figure 15). As seen in Figure 16 the optimized tool path case is more suitable; however, in this case, heat localization takes place in the center of the component leaving the rest of the component (arms) at relatively low temperatures. As it will be further discussed, these differences have important consequences on the microstructure and the mechanical state of the final component.

Having obtained the temperature evolution, the stored temperature data $\theta(\vec{x}, t)$ at each node of the finite element mesh was used to evaluate the phase fraction evolution of the four phases (austenite, ferrite, bainite, martensite) as presented in Sec. 2.2 of the metallurgical solver. In the following (Figures 17 and 18), the phase volume fractions for the as-built components after the temperatures have equilibrated with the room temperature is presented. *The completed evolution of the phases is captured in a movie provided in the supplementary information.*

From Figure 17 of the uniform tool path case, it is noticed that the overall distribution of the phases

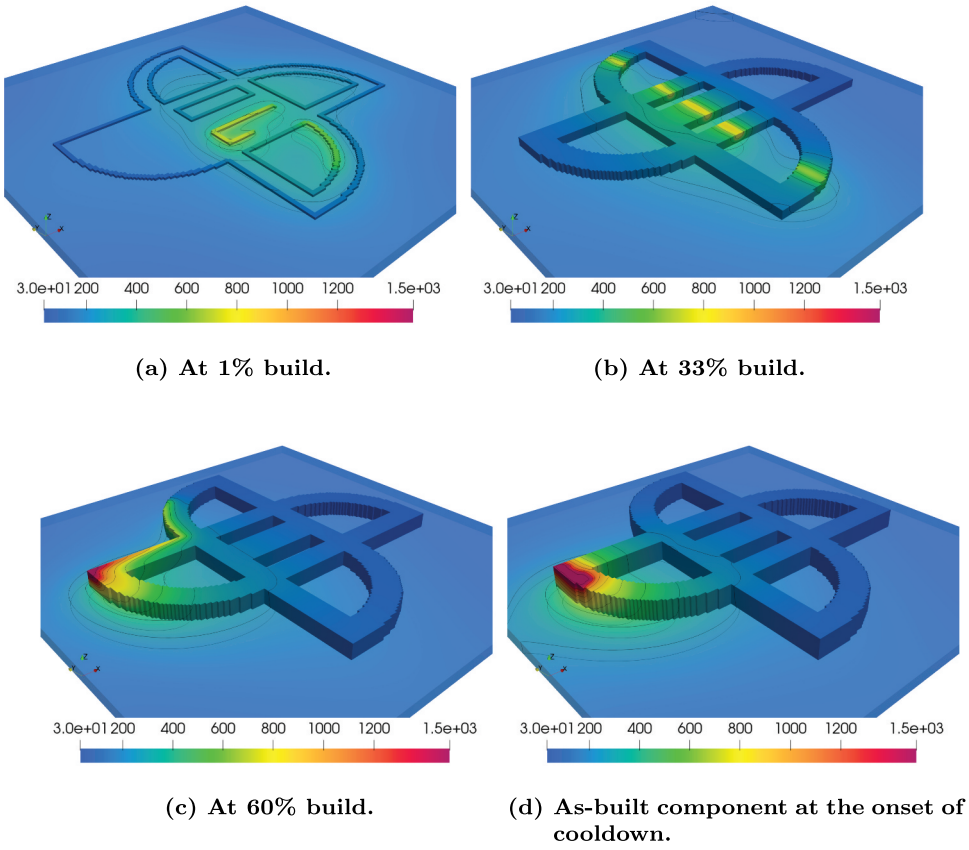


(a) At 1% build. (b) At 33% build.

(c) At 60% build. (d) As-built component at the onset of cooldown.

Figure 15. Temperature field evolution during the build of the windmill geometry with uniform toolpath. Temperature range is (30–1500) °C.

strongly resembles the deposition path, where each pass is visible for instance in terms of ferrite and bainite volume fractions (panels (a) and (b)). At the same time, martensite (panel (c)) appears with smaller volume fraction, present mostly in the two arms region.

Inspection of Figure 18, where the results with the optimized tool path are shown, elucidates important differences compared to the reference tool path. Using the optimized tool path, volume fractions appear more uniformly distributed. This result was interpreted by noting that the optimized tool path builds each feature (arms and connectors among them) in a sequential rather than parallel manner, one by one. Since each feature has about the same size, each experiences a similar history and, consequently, results in a similar phase distribution. At the same time, most of the ferrite is located in the central region where slower cooling rates were observed. The remaining 'arms' are mostly bainitic. Martensite is also present mostly in the regions near the baseplate due to high cooling rates during the first deposition passes on the 'cold' baseplate, similarly to case of the thin wall.

### 5.2. Microstructure-informed mechanical solver

As detailed in Sec. 2, the solver is informed by both the temperature evolution as well as the local microstructure, which dictates local mechanical properties (see Figure 4).

Subjected to boundary conditions where the bottom plane of the baseplate is mechanically fixed ($u = v = w = 0$), the total distortion, accumulated equivalent plastic strain, and von-Mises stress during the build-up and the cool-down step were investigated. The results of the as-built windmills are presented in Figures 19 and 20. *A complete evolution is captured in a movie provided in the supplementary information.*

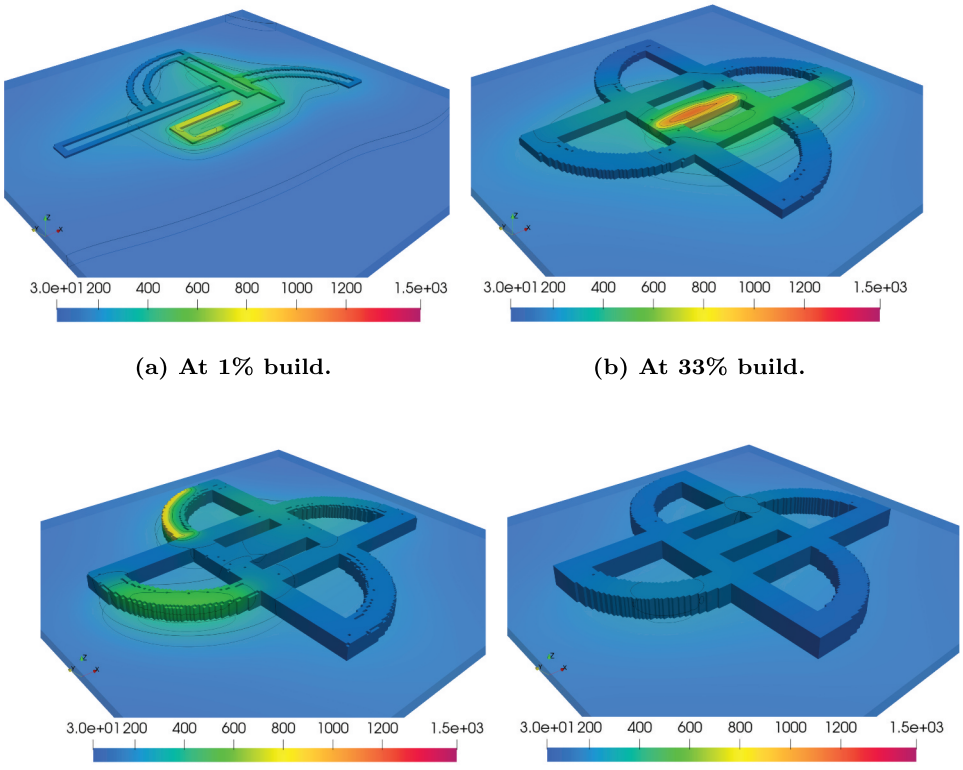


(a) At 1% build. (b) At 33% build.

(c) At 60 % build. (d) As-built component at the onset of cooldown.

**Figure 16.** Temperature field evolution during the build of the windmill geometry with optimized toolpath. Temperature range is (30–1500) °C.

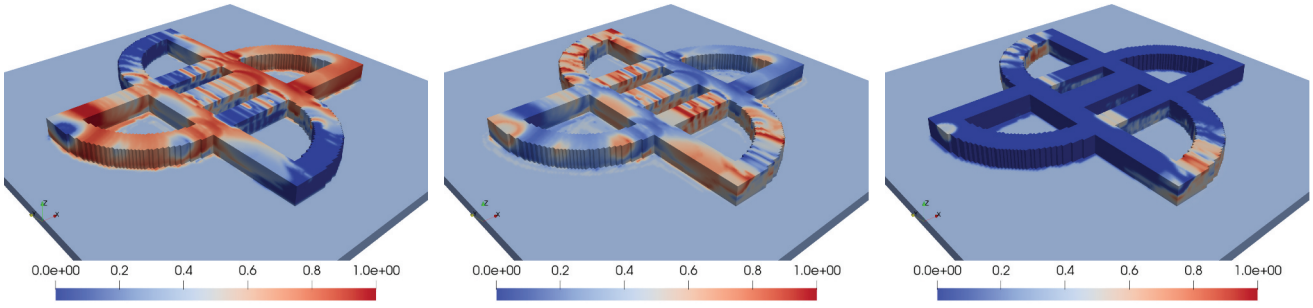


(a) Volume fraction of ferrite. (b) Volume fraction of bainite. (c) Volume fraction of martensite.

**Figure 17.** Phase volume fraction of ferrite, bainite and martensite in the printed windmill (uniform toolpath).

Analysis of the displacement field reveals that the maximum displacement along the build direction is in both cases below 300$\mu m$. However, the overall distortion patterns are significantly different as they are derived from different sequences of deposition. A more wavy-like pattern is observed in Figure 19(a) following the uniform tool path, while a more feature-based pattern (along the edges of the arms) is observed in Figure 20(a) of the optimized tool path. The overall distortion is

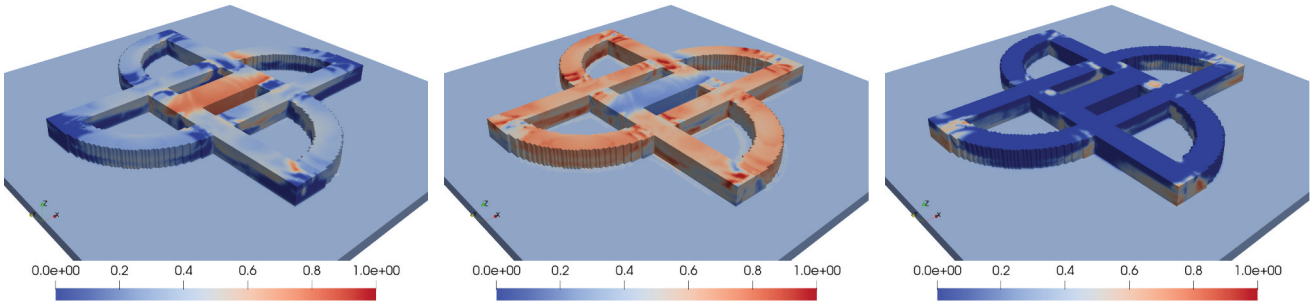


(a) Volume fraction of ferrite. (b) Volume fraction of bainite. (c) Volume fraction of martensite.

Figure 18. Phase volume fraction of ferrite, bainite and martensite in the printed windmill (optimized toolpath).

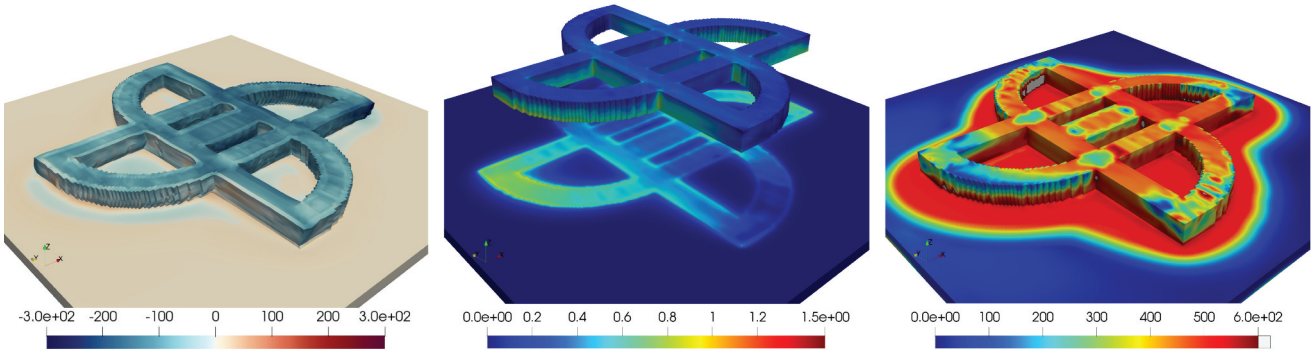


(a) Displacement $w$ [$\mu$m]. Deformation is 8$\times$ magnified. (b) Accumulated equivalent plastic strain $\bar{\varepsilon}^p$. (c) Von-Mises stress $\sigma_{eq}$ [MPa].

Figure 19. Result of the (left) displacement field, (middle) accumulated equivalent plastic strain, (right) von-mises stress for the windmill geometry with the uniform toolpath.

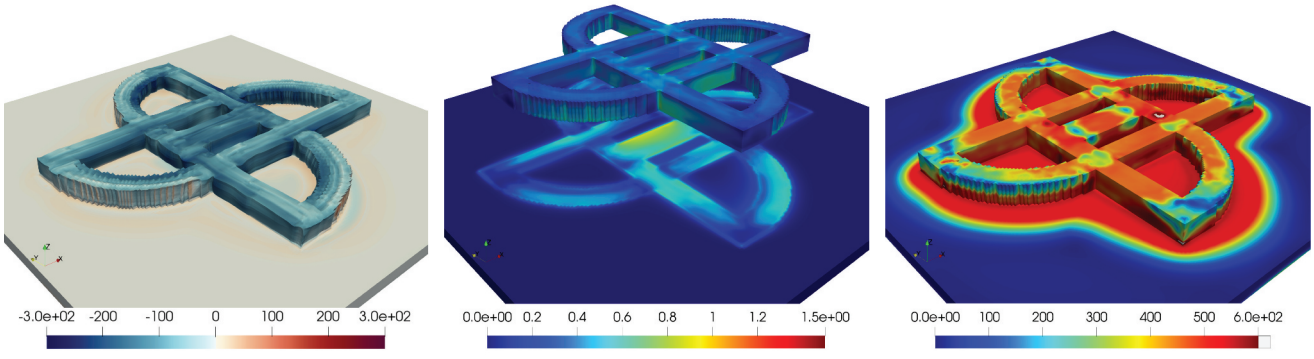


(a) Displacement $w$ [$\mu$m]. Deformation is 8$\times$ magnified. (b) Accumulated equivalent plastic strain $\bar{\varepsilon}^p$. (c) Von-Mises stress $\sigma_{eq}$ [MPa].

Figure 20. Result of the (left) displacement field, (middle) accumulated equivalent plastic strain, (right) von-mises stress for the windmill geometry with the optimized toolpath.

the complex outcome of the concurrent volume changes arising from the thermal shrinkage and from microstructure phase transformations.

The accumulated plastic strain is plotted in the center part of Figures 19 and 20. To better visualize the critical regions of the total accumulated equivalent plastic strain, the component is separated from the baseplate and move it upwards (this was purely a visualization analysis, not a simulation step). This reveals the equivalent plastic strain distribution at the top of the baseplate. In the uniform tool path case, plastic deformation accumulates mostly in the arms of the windmill, while in the optimized case, it remains concentrated near the center. While the accumulated plastic strain may be considered as a first-order approximation revealing the potential damage sites due to ductile failure, it should be highlighted that a more detailed analysis would require a more complex plasticity (damage) model incorporating the ongoing in-situ annealing on the evolution of dislocation density.

Similarly, in the right part of Figures 19 and 20, residual von-Mises stress distribution patterns can also be attributed to the overall deposition sequence and phase microstructure. The homogeneous stress pattern in the baseplate is due to its uniform microstructure largely unaffected by the deposition, while the non-uniform pattern in the component is an indication of the coexistence of various phases of different mechanical properties.

## 6. Conclusion

In conclusion, an in-house simulation capability that integrates thermal, metallurgical, and mechanical solvers in a sequential manner to model the directed energy deposition (DED) of EH36 steel components was developed. The framework incorporates finite element solvers for thermal and mechanical analysis, complemented by a phase fraction model specifically chosen for its computational efficiency and seamless integration with the finite element solvers. The simulation inputs require STL files for the component and baseplate, as well as g-code. Through this study, the potential of utilizing such a framework in the context of directed energy deposition, primarily focusing on evaluating the impact of robot tool path on the quality of fabricated parts, was demonstrated. Because the framework is specifically tailored to EH36 material, it is limited in material applicability, in its current form, to steels. Application to a steel grade other than EH36 would require a reparameterization of the microstructure model as well as thermal and mechanical properties of the alloy.

Verification tests were conducted, and printing of a windmill geometry was simulated. The results indicate that a tool path optimized for printing speed may not necessarily result in significant effects on phases, residual stresses, and distortion distribution. Interestingly, it was observed that a shorter 'power-off' time can improve microstructure uniformity to some extent, but does not achieve complete uniformity. This finding highlights the need for further work involving explicit optimization through a closed-feedback loop.

Moreover, from the material's perspective, the results indicate that, when used in DED, the microstructure of EH36 predominantly consists of bainite, with smaller volume fractions of ferrite and some martensite concentrated near the baseplate.

By presenting this integrated framework, this work underscores the significance of digital modeling as a valuable tool for component and process development in directed energy deposition of large-format metallic components.

## Disclosure statement

The authors have no relevant financial or non-financial interests to disclose.

## Funding

This work was supported by the Agency for Science, Technology and Research (A*STAR) with Grants "Integrated Large Format Hybrid Manufacturing using Wire-fed and Powder-blown Technology for LAAM process" (A1893a0031), "Industrial Digital Design and Additive Manufacturing Workflows" (A19E1a0097), and "Advanced Models for Additive Manufacturing ($AM^2$) (M22L2b0111).

## ORCID

Jakub Mikula http://orcid.org/0000-0002-4964-8129
Guglielmo Vastola http://orcid.org/0000-0003-2101-6178

## Data availability statement

The raw data that support the findings of this study are available from the corresponding authors.

## References


Ali, B., Y. Heider, and B. Markert. 2023. "Modeling the Thermomechanical Processes and Residual Stresses in Additive Manufacturing of Metallic Components." *PAMM* 22 (1): e202200089. https://doi.org/10.1002/pamm.202200089.

Ali, M. H., and Y. Sung Han. 2021. "Effect of Phase Transformations on Scanning Strategy in WAAM Fabrication." *Materials* 14 (24): 7871. https://doi.org/10.3390/ma14247871.

Avrami, M. 2004. "Granulation, Phase Change, and Microstructure Kinetics of Phase Change. III." *Journal of Chemical Physics* 9 (2): 177–184. https://doi.org/10.1063/1.1750872.

Baykasoğlu, C., A. Oncu, T. Merve, and C. T. Albert. 2020. "A Process- Microstructure Finite Element Simulation Framework for Predicting Phase Transformations and Microhardness for Directed Energy Deposition of Ti6Al4V." *Additive Manufacturing* 35:101252. https://doi.org/10.1016/j.addma.2020.101252.

Belytschko, T., W. K. Liu, and B. Moran. 2000. *Nonlinear Finite Elements for Continua and Structures*. Nonlinear Finite Elements for Continua and Structures. Wiley. https://books.google.com.sg/books?id=C6goAQAAMAAJ.

Bennett, J. L., O. L. Kafka, H. Liao, S. J. Wolff, Y. Cheng, P. Cheng, G. Hyatt, K. Ehmann, and J. Cao. 2018. "Cooling Rate Effect on Tensile Strength of Laser Deposited Inconel 718." *Procedia Manufacturing* 26:912–919. 46th SME North American Manufacturing Research Conference, NAMRC 46, Texas, USA. https://doi.org/10.1016/j.promfg.2018.07.118.

Bonnín Roca, J., P. Vaishnav, R. E. Laureijs, J. Mendonc¸a, and R. H. F. Erica. 2019. "Technology Cost Drivers for a Potential Transition to Decentralized Manufacturing." *Additive Manufacturing* 28:136–151. https://doi.org/10.1016/j.addma.2019.04.010.

Chew, Y., J. Hock Lye Pang, B. Guijun, and B. Song. 2015. "Thermo-Mechanical Model for Simulating Laser Cladding Induced Residual Stresses with Single and Multiple Clad Beads." *Journal of Materials Processing Technology* 224:89–101. https://doi.org/10.1016/j.jmatprotec.2015.04.031.

Chiumenti, M., X. Lin, M. Cervera, W. Lei, Y. Zheng, and W. Huang. 2017. "Numerical Simulation and Experimental Calibration of Additive Manufacturing by Blown Powder Technology. Part I: Thermal Analysis." *Rapid Prototyping Journal* 23 (2): 448–463. https://doi.org/10.1108/RPJ-10-2015-0136.

Costa, L., R. Vilar, T. Reti, and A. M. Deus. 2005. "Rapid Tooling by Laser Powder Deposition: Process Simulation Using Finite Element Analysis." *Acta Materialia* 53 (14): 3987–3999. https://doi.org/10.1016/j.actamat.2005.05.003.

Costello, S. C. A., C. R. Cunningham, X. Fangda, A. Shokrani, V. Dhokia, and S. T. Newman. 2023. "The State-Of-The-Art of Wire Arc Directed Energy Deposition (WA-DED) as an Additive Manufacturing Process for Large Metallic Component Manufacture." *International Journal of Computer Integrated Manufacturing* 36 (3): 469–510. https://doi.org/10.1080/0951192X.2022.2162597.

Dietrich, D. M., M. Kenworthy, and E. A. Cudney. 2019. *Additive Manufacturing Change Management: Best Practices*. Boca Raton, United States: CRC Press.

Gabriel, E., G. E. Fagg, G. Bosilca, T. Angskun, J. J. Dongarra, J. M. Squyres, and V. Sahay, et al. 2004. "Open MPI: Goals, Concept, and Design of a Next Generation MPI Implementation." In *Proceedings, 11th European PVM/MPI Users' Group Meeting*, Budapest, Hungary, September, 97–104.

Gouge, M., and P. Michaleris. 2018. *Thermo-Mechanical Modeling of Additive Manufacturing*. Amsterdam, Netherlands: Elsevier.

Guennebaud, G., and B. Jacob. 2010. "Eigen v3." http://eigen.tuxfamily.org.

Han, Y. S., K. Lee, M.-S. Han, H. Chang, K. Choi, and I. Seyoung. 2011. "Finite Element Analysis of Welding Processes by Way of Hypoelasticity- Based Formulation." *Journal of Engineering Materials and Technology* 133 (2): 021003. https://doi.org/10.1115/1.4003099.

Heigel, J. C., P. Michaleris, and E. W. Reutzel. 2015. "Thermo-Mechanical Model Development and Validation of Directed Energy Deposition Additive Manufacturing of Ti–6Al–4V." *Additive Manufacturing* 5:9–19. https://doi.org/10.1016/j.addma.2014.10.003.

Kaierle, S., L. Overmeyer, I. Alfred, B. Rottwinkel, J. Hermsdorf, V. Wesling, and N. Weidlich. 2017. "Single-Crystal Turbine Blade Tip Repair by Laser Cladding and Remelting." *CIRP Journal of Manufacturing Science and Technology* 19:196–199. https://doi.org/10.1016/j.cirpj.2017.04.001.

Koistinen, D. P., and R. E. Marburger. 1959. "A General Equation Prescribing the Extent of the Austenite-Martensite Transformation in Pure Iron-Carbon Alloys and Plain Carbon Steels." *Acta Metallurgica* 7 (1): 59–60. https://doi.org/10.1016/0001-6160(59)90170-1.

Kooiker, H., E. S. Perdahcıoğlu, and A. H. van den Boogaard. 2020. "Combined Athermal and Isothermal Martensite to Austenite Reversion Kinetics, Experiment and Modelling." *Materials & Design* 196:109124. https://doi.org/10.1016/j.matdes.2020.109124.

Labudovic, M., H. Dongming, and R. Kovacevic. 2003. "A Three Dimensional Model for Direct Laser Metal Powder Deposition and Rapid Prototyping." *Journal of Materials Science* 38 (1): 35–49. https://doi.org/10.1023/A:1021153513925.

Leblond, J. B., and J. Devaux. 1984. "A New Kinetic Model for Anisothermal Metallurgical Transformations in Steels Including Effect of Austenite Grain Size." *Acta Metallurgica* 32 (1): 137–146. https://doi.org/10.1016/0001-6160(84)90211-6.

Lee, S.-J., M. T. Lusk, and Y.-K. Lee. 2007. "Conversional Model of Transformation Strain to Phase Fraction in Low Alloy Steels." *Acta Materialia* 55 (3): 875–882. https://doi.org/10.1016/j.actamat.2006.09.008.

Liu, N., K. Ren, W. Zhang, Y. F. Zhang, Y. X. Chew, G. J. Bi, and J. Y. H. Fuh. 2021. "An Evolutional Algorithm for Automatic

2D Layer Segmentation in Laser-Aided Additive Manufacturing." *Additive Manufacturing* 47:102342. https://doi.org/10.1016/j.addma.2021.102342.

Lu, X., M. Cervera, M. Chiumenti, L. Junjie, J. Xianglin, G. Zhang, and X. Lin. 2020. "Modeling of the Effect of the Building Strategy on the Thermomechanical Response of Ti-6Al-4V Rectangular Parts Manufactured by Laser Directed Energy Deposition." *Metals* 10 (12): 1643. https://doi.org/10.3390/met10121643.

Lu, X., M. Chiumenti, M. Cervera, G. Zhang, and X. Lin. 2022. "Mitigation of Residual Stresses and Microstructure Homogenization in Directed Energy Deposition Processes." *Engineering with Computers* 38 (6): 4771–4790. https://doi.org/10.1007/s00366-021-01563-9.

Merve, T., A. Oncu, B. Cengiz, and C. T. Albert. 2023. "A Fully Coupled Thermal–Microstructural–Mechanical Finite Element Process Model for Directed Energy Deposition Additive Manufacturing of Ti–6Al–4V." *Science and Technology of Welding and Joining* 28 (2): 118–127. https://doi.org/10.1080/13621718.2022.2127211.

Peyre, P., P. Aubry, R. Fabbro, R. Neveu, and A. Longuet. 2008. "Analytical and Numerical Modelling of the Direct Metal Deposition Laser Process." *Journal of Physics D: Applied Physics* 41 (2): 025403. https://doi.org/10.1088/0022-3727/41/2/025403.

Piekarska, W., M. Kubiak, and M. Zmindak. 2017. "Issues in Numerical Modeling of Phase Transformations in Welded Joint." *Procedia Engineering* 177:141–148. XXI PolishSlovak Scientific Conference Machine Modeling and Simulations MMS 2016.September 6-8, 2016, Hucisko, Poland https://doi.org/10.1016/j.proeng.2017.02.204.

Ren, K., Y. Chew, J. Y. H. Fuh, Y. F. Zhang, and G. J. Bi. 2019. "Thermo-Mechanical Analyses for Optimized Path Planning in Laser Aided Additive Manufacturing Processes." *Materials & Design* 162:80–93. https://doi.org/10.1016/j.matdes.2018.11.014.

Rong, Y., T. Lei, X. Jiajun, Y. Huang, and C. Wang. 2018. "Residual Stress Modelling in Laser Welding Marine Steel EH36 Considering a Thermodynamics-Based Solid Phase Transformation." *International Journal of Mechanical Sciences* 146- 147:180–190. https://doi.org/10.1016/j.ijmecsci.2018.07.046.

Schroeder, W., K. Martin, and B. Lorensen. 2006. *The Visualization Toolkit*. : Kitware.

SIEMENS. 2018. *SINUMERIK Operate*. https://static.dc.siemens.com/cnc4you/CNC-Downloads/SINUMERIK-Operate-UserGuide-2013-09-bw-en.pdf.

Simo, J. C., and R. L. Taylor. 1985. "Consistent Tangent Operators for Rate-Independent Elastoplasticity." *Computer Methods in Applied Mechanics and Engineering* 48 (1): 101–118. https://doi.org/10.1016/0045-7825(85)90070-2.

Stender, M. E., L. L. Beghini, J. D. Sugar, M. G. Veilleux, S. R. Subia, T. R. Smith, C. W. S. San Marchi, A. A. Brown, and D. J. Dagel. 2018. "A Thermal-Mechanical Finite Element Workflow for Directed Energy Deposition Additive Manufacturing Process Modeling." *Additive Manufacturing* 21:556–566. https://doi.org/10.1016/j.addma.2018.04.012.

Strickland, J. D. 2016. "Applications of Additive Manufacturing in the Marine Industry." *Proceedings of PRADS2016*, Hotel Crowne Plaza, Copenhagen, Denmark.

The Trilinos Project Team. 2020. The Trilinos Project Website. https://trilinos.github.io

Wang, J., Y. Xiang Chew, W. Wen Jin, W. Jing, X. Tan, E. Liu, B. Guijun, et al. 2021. "Microstructure and Mechanical Properties of ASTM A131 EH36 Steel Fabricated by Laser Aided Additive Manufacturing." *Materials Characterization* 174:110949. https://doi.org/10.1016/j.matchar.2021.110949.

Weisz-Patrault, D. 2020. "Fast Simulation of Temperature and Phase Transitions in Directed Energy Deposition Additive Manufacturing." *Additive Manufacturing* 31:100990. https://doi.org/10.1016/j.addma.2019.100990.

Ya, W., and K. Hamilton. 2018. "On-Demand Spare Parts for the Marine Industry with Directed Energy Deposition: Propeller Use Case". *Proceedings of the Additive Manufacturing in Products and Applications*. Springer. https://doi.org/10.1007/978-3-319-66866-6_7.

Yang, Q., P. Zhang, L. Cheng, Z. Min, M. Chyu, and A. C. To. 2016. "Finite Element Modeling and Validation of Thermomechanical Behavior of Ti-6Al-4V in Directed Energy Deposition Additive Manufacturing." *Additive Manufacturing* 12:169–177. Special Issue on Modeling & Simulation for Additive Manufacturing. https://doi.org/10.1016/j.addma.2016.06.012.

Zheng, B., J. C. Haley, N. Yang, J. Yee, K. W. Terrassa, Y. Zhou, E. J. Lavernia, and J. M. Schoenung. 2019. "On the Evolution of Microstructure and Defect Control in 316L SS Components Fabricated via Directed Energy Deposition." *Materials Science and Engineering: A* 764:138243. https://doi.org/10.1016/j.msea.2019.138243.

Zou, X., D. Zhao, J. Sun, C. Wang, and H. Matsuura. 2018. "An Integrated Study on the Evolution of Inclusions in EH36 Shipbuilding Steel with Mg Addition: From Casting to Welding." *Metallurgical and Materials TransactionsB* 49 (2): 481–489. https://doi.org/10.1007/s11663-017-1163-x.